ELSEVIER

J. Non-Newtonian Fluid Mech. 97 (2001) 207–232

Journal of Non-Newtonian Fluid Mechanics

www.elsevier.com/locate/jnnfm

The flow of viscoelastic fluids past a cylinder: finite-volume high-resolution methods

M.A. Alves [a], F.T. Pinho [b], P.J. Oliveira [c,*]

[a] *Departamento de Engenharia Química, CEFT, Faculdade de Engenharia da Universidade do Porto, Rua Roberto Frias, 4200-465 Porto, Portugal*

[b] *Centro de Estudos de Fenómenos de Transporte, Faculdade de Engenharia da Universidade do Porto, Rua dos Bragas, 4050-123 Porto, Portugal*

[c] *Departamento de Engenharia Electromecânica, Universidade da Beira Interior, Rua Marques D'Avila e Bolama, 6200 Covilhã, Portugal*

Received 13 June 2000; received in revised form 6 November 2000

Abstract

Accurate solutions are obtained with the numerical method of Oliveira et al. [J. Non-Newtonian Fluid Mech. 79 (1998) 1] for the inertialess plane flow around a confined cylinder. This numerical procedure is based on the finite-volume method in non-orthogonal block-structured meshes with a collocated arrangement of the dependent variables, and makes use of a special interpolation practice to avoid stress–velocity decoupling. Two high-resolution schemes (MINMOD and SMART) are implemented to represent the convective terms in the constitutive equations for the upper convected Maxwell and Oldroyd-B fluids, and the resulting predictions of the drag coefficient on the cylinder are shown to be as accurate as existing finite-element method predictions based on the supposedly very accurate h-p refinement technique. Numerical uncertainties are quantified with help of Richardson's extrapolation technique and the orders of convergence of the differencing schemes are established and shown to be second-order accurate. Calculations performed with a wake-refined mesh predicted the variation of the maximum longitudinal normal stress in the wake as De^3 and De^5 depending on Deborah number.

Keywords: Finite-volume; High-resolution; Cylinder; Viscoelastic; MINMOD; SMART

1. Introduction

The flow past arrays of cylinders and rod bundles is industrially relevant regardless of the type of fluid: Newtonian fluids with low and high viscosity are found under turbulent and laminar flows in heat exchangers for energy generation and distribution [2], or in manufacturing processes [3]. Viscoelastic fluids are also found in applications involving flows around cylinders, as in district heating and cooling

* Corresponding author. Fax: +351-275-320820.
E-mail addresses: mmalves@fe.up.pt (M.A. Alves), fpinho@fe.up.pt (F.T. Pinho), pjpo@ubi.pt (P.J. Oliveira).

0377-0257/01/$ – see front matter
PII: S0377-0257(00)00198-1

systems [4], food processes, porous media flows and other areas of process engineering [5], and more specifically in enhanced oil recovery [6] or the coating of fibres.

The increasing use of computational tools to design industrial equipment requires the ability of existing methods to predict accurately the flow of viscoelastic fluids and in this respect one of the relevant benchmark test cases is the two-dimensional flow around a cylinder [7]. This flow is classified as a "smooth flow", because it does not possess any geometrical singularity, such as a re-entrant corner, but this does not mean that it is an easy flow to predict: difficulties associated with the development of thin stress layers on the cylinder surface and along the centreline in the cylinder wake, restrict the range of Deborah numbers (*De*) for which steady solutions are obtained.

Efforts on the development of better finite-element methods (FEM) for the prediction of viscoelastic flows are continuously being made and some new FEM have recently been tested against this benchmark problem. Recent works (1998/1999) involving simulation of the flow around a confined cylinder are those of Liu et al. [8], Fan et al. [9], Sun et al. [10] and Dou and Phan-Thien [11]. Liu et al. [8] review some of the most relevant experimental and numerical works for flows past arrays of cylinders and past a single cylinder. The paper by Sun et al. [10] provides a very clear summary of the most important steps in recent developments of finite-element based methods for the prediction of viscoelastic fluids, and in particular the various formulations for splitting the momentum and constitutive equations aimed at improving the numerical stability of the procedures. On the other hand, the numerical investigation of Dou and Phan-Thien [11] with the control volume-based finite element metod (CVFEM) has analysed in some detail the various contributions to the drag force in a tentative to better understand the observed and predicted variations of drag coefficient with the Deborah number. These authors have used various formulations of FEM and, as we shall see, the accuracy of the resulting prediction of the drag force on the cylinder is also variable.

Finite-volume methods (FVM) are serious alternatives to FEM for viscoelastic computations as they offer advantages in terms of computing resources (Huang et al. [12]). None better than Phan-Thien and co-workers in this judgement as they have been developing simultaneously several numerical procedures based on FVM (e.g. Xue et al. [13]), on FEM (e.g. Fan et al. [9]), and on CVFEM (e.g. Huang et al. [12] and Dou and Phan-Thien [11]) which is an hybrid approach of FEM and FVM. In any case, far less effort has been dedicated to the development of FVM techniques for viscoelastic flow predictions, at least when judged on the number of publications and the performance of the codes. The present paper reports, improvements to one such FVM and shows that, it is as capable and accurate as advanced FEM methods to predict the viscoelastic flow around a cylinder. The paper also confirms, in an independent way, results obtained by some FEM simulations (namely those of [9]).

To our best knowledge, the first simulation of viscoelastic flow around an unbounded cylinder with a finite-volume based method was carried out by Hu and Joseph [14], who relied on the staggered mesh arrangement and first-order interpolation schemes for stress and momentum convection. The staggered arrangement is difficult to generalise to complex geometries and first-order interpolation schemes are known to give rise to inaccuracies due to artificial diffusion. Other finite-volume calculations have been performed and assessed on the basis of either the well-known 4:1 contraction flow, such as those by Yoo and Na [15], Sasmal [16] and Xue et al. [13], or straight flows in rectangular cross-section ducts (Gervang and Larsen [17]); all these studies relied again on the staggered approach in orthogonal meshes for coupling pressure and velocity, and thus, offer limited scope for application to complex geometries requiring general non-orthogonal meshes.

A general collocated FVM procedure for viscoelastic flows has been developed by Oliveira et al. [1] for semi-structured grids, thus, allowing the mapping of complex geometries. These authors have

also performed simulations with formally second-order interpolation schemes for the discretisation of the convective terms in the constitutive equation. That method was especially developed for collocated, generally non-orthogonal, grids and has been subsequently improved in a number of points: a variation to the original interpolation technique for the cell face stresses was introduced and tested by Pinho and Oliveira [18], and an extensive investigation of the advantages and shortcomings of the application of second-order upwinding to the convective terms in the constitutive equation was carried out by the same authors [19]. In this latter study, it became apparent that in order to improve the stability of the method and accuracy of the predictions one had to resort to bounded high-resolution interpolation schemes and that has been accomplished by Alves et al. [20] who demonstrated the method with the difficult 4:1 plane contraction flow. In the present paper, a second, more accurate high-resolution interpolation scheme for convection is implemented for enhanced accuracy and the formulation is tested with the benchmark problem of the flow past a confined cylinder (blockage ratio 0.5), with both upper convected Maxwell (UCM) and Oldroyd-B fluids. This smooth problem requires non-orthogonal meshes and allows comparison of the drag force on the cylinder (the benchmark result) with values from other simulation in the literature [8–11], thus enabling a direct assessment of the accuracy of the present FVM.

Section 2 presents the governing equations and the implementation of the high-resolution schemes into the finite-volume method is explained in Section 3. Section 4 defines the configuration and computational meshes used to study the flow around a bounded cylinder and in Section 5, the results of the simulations are presented and discussed.

2. Governing equations

The method solves the system of equations for incompressible flow, made up of conservation of mass and of linear momentum:

$$\frac{\partial u_i}{\partial x_i} = 0, \tag{1}$$

$$\frac{\partial(\rho u_i)}{\partial t} + \frac{\partial(\rho u_j u_i)}{\partial x_j} = -\frac{\partial p}{\partial x_i} + \frac{\partial \tau_{ij_{\text{tot}}}}{\partial x_j}, \tag{2}$$

and the rheological constitutive model for an Oldroyd-B fluid which is written as follows:

$$\tau_{ij_{\text{tot}}} = \eta_{\text{s}}\left(\frac{\partial u_i}{\partial x_j} + \frac{\partial u_j}{\partial x_i}\right) + \tau_{ij}, \tag{3a}$$

$$\tau_{ij} + \lambda\left(\frac{\partial \tau_{ij}}{\partial t} + \frac{\partial u_k \tau_{ij}}{\partial x_k}\right) = \eta_{\text{P}}\left(\frac{\partial u_i}{\partial x_j} + \frac{\partial u_j}{\partial x_i}\right) + \lambda\left(\tau_{jk}\frac{\partial u_i}{\partial x_k} + \tau_{ik}\frac{\partial u_j}{\partial x_k}\right), \tag{3b}$$

where Einstein's summation convention applies, ρ is the density of the fluid, u_i the velocity component along the Cartesian co-ordinate x_i, p the pressure, λ the relaxation time, η_{s} the shear viscosity of the Newtonian solvent and η_{P} the contribution of the polymer to the total shear viscosity $\eta = \eta_{\text{s}} + \eta_{\text{P}}$. The upper convected Maxwell model is recovered in this formulation by setting $\eta_{\text{s}} = 0$. The dependent variables solved for in Eqs. (3) are the polymer stress components τ_{ij} and there is no need to store the total stress $\tau_{ij_{\text{tot}}}$.

Although we are here concerned with steady flows, the numerical method approaches that steady-state by a time marching sequence, so the inertia term in Eqs. (2) and (3b) are retained. This time-marching approach offers the advantage of being able to capture possible unsteady phenomena. It is also noted that we adopt the notation of writing on the left-hand side of Eqs. (2) and (3b) the terms which will be dealt with implicitly in the numerical procedure, and on the right-hand side those dealt with explicitly (these go into the source term of the matrix equations).

3. Numerical method

The equations of the previous section are transformed into a general non-orthogonal co-ordinate system for easy application of the FVM method to a collocated mesh arrangement. The equations are then integrated over the set of control volumes (cells) and discretised. The dependent variables remain the Cartesian velocity and polymer stress components and the pressure, all stored at the centre of the cells. To avoid stress–velocity decoupling, the special procedure developed in the previous work [1,18] is adopted for the calculation of the divergence of the stress term in the momentum equation; an abridged explanation of the procedure followed is given at the end of Section 3.1 and other details can be found in the above references. The new issue here is the implementation of the high-resolution schemes used to discretise the convective terms in the constitutive equation and only this will be addressed in detail below.

3.1. Constitutive equation

After discretisation the constitutive Eq. (3b) for a general cell P of volume V_P is written under a linearised form as

$$a_P \tau_{ij,P} - \sum_F^6 a_F \tau_{ij,F} = S_{\tau_{ij}} + \frac{\lambda_P V_P}{\delta t} \tau^0_{ij,P}, \tag{4}$$

where $\tau_{ij,P}$ is the stress in the cell, $\tau_{ij,F}$ stresses in neighbouring cells and δt the time step. Superscript '0' denotes values at the previous time level and since the iterative-like time advancement is fully implicit, absence of superscript denotes new time level values. As there is no diffusion term in the original constitutive equation, the coefficients a_F are composed by convective contributions only. When these convective coefficients are based on the upwind differencing scheme (UDS), the following form results for the a_F coefficients:

$$a_F = -\frac{\lambda}{\rho} \min(F_f, 0), \tag{5}$$

where F_f represents the mass flow rate across the face 'f' between cells P and F, which is evaluated as described in Issa and Oliveira [21]. The convective terms are not, however, discretised with UDS, but with the high-resolution schemes (HRS) to be described in the next section. This will not change the coefficients of the stress equation, which are still based on Eq. (5), and the effect of the HRS will be introduced through the deferred correction approach [22] as explained in our previous work [20]. This approach is very convenient because allows for a unified implementation of various HRS. Basically, the convective fluxes based on the HRS are treated explicitly and inserted into the source term of the

discretised stress equations, after being subtracted from the corresponding fluxes based on UDS. As a steady solution is attained, the explicit fluxes based on UDS cancel out with the implicit fluxes embedded in the coefficients, and thus, what remains is the contribution from the HRS fluxes, as wanted.

The remaining terms in the discretised Eq. (4) are the central coefficient, given by

$$a_{\mathrm{P}} = V_{\mathrm{P}} + \sum_{\mathrm{F}}^{6} a_{\mathrm{F}} + \frac{\lambda V_{\mathrm{P}}}{\delta t} \tag{6}$$

and the source term, which will incorporate the following three contributions:

1. part of the Oldroyd derivative on the right-hand side of Eq. (3b), which is evaluated with the central differencing scheme (CDS);
2. the viscous part of the stresses, also evaluated with CDS; and
3. the additional term due to implementation of the high-resolution scheme by deferred correction, which is given by the difference between convected stress fluxes based on HRS and those based on UDS.

For the sake of completeness, we give now some details of the stress–velocity coupling procedure [1,18]. In the differential momentum equation (Eq. (2)) the stress–divergence term is $\partial \tau_{ij}/\partial x_j$ and, in the integrated finite-volume equations, this becomes a sum of stress force vectors acting on each cell face, $\sum_j^3 B_{\mathrm{f}j}\tau_{ij,\mathrm{f}}$ ($B_{\mathrm{f}j}$ are components of the cell face area). If the τ_{ij} were linearly interpolated to a cell face 'f' to obtain $\tau_{ij,\mathrm{f}}$, a decoupling similar to the well-known checkerboard pressure/velocity decoupling problem would occur (see [1]). In order to resolve this problem, and following references [1,18], we first recast Eq. (4) under the form:

$$\tau_{ij} = \sum_{l}^{3} (b_{li}[\Delta u_j]_l + b_{lj}[\Delta u_i]_l) + S'_{\tau_{ij}},$$

where terms on velocity differences $[\Delta u_i]_l$ (with $l = 1$–3 denoting the mesh line directions) are explicitly written, while all the others are absorbed into $S'_{\tau_{ij}}$, and the b_{li} are obtained by comparison with the original Eq. (4) after expanding the source term, $S_{\tau_{ij}}$. Then, the cell face stress value is obtained from

$$\tau_{ij,\mathrm{f}} = b_{\mathrm{f}i}[\Delta u_j]_{\mathrm{f}} + b_{\mathrm{f}j}[\Delta u_i]_{\mathrm{f}} + \overline{\sum_{l\neq \mathrm{f}}^{2} (b_{li}[\Delta u_j]_l + b_{lj}[\Delta u_i]_l) + S'_{\tau_{ij}}},$$

where all terms are linearly interpolated (indicated by the overbar) except those proportional to velocity differences straddling cell face 'f' which are directly evaluated as a difference between values of the adjacent cells, $[\Delta u_i]_{\mathrm{f}} = u_{i,\mathrm{F}} - u_{i,\mathrm{P}}$. It has been shown in [1] that this practice prevents stress and velocity oscillations, by coupling the stress at any cell face directly with the surrounding velocities, and that it also leads to faster iterative convergence.

3.2. High-resolution diferencing schemes

In the FV method the convective terms in the constitutive equations are integrated over a cell and, after application of Gauss' theorem, one ends up with a balance of convective stress fluxes, $F_{\mathrm{f}}\hat{\tau}_{ij,\mathrm{f}}$. The cell face value of the stress, $\hat{\tau}_{ij,\mathrm{f}}$, needs to be specified in terms of surrounding nodal stress values

by means of an appropriate interpolation scheme. Oliveira and Pinho [19] have shown that the use of high-order schemes to determine those stress values, such as the linear-upwind differencing scheme (LUDS) which is formally second-order, results in improved accuracy of the numerical solutions as compared with straightforward application of the upwind differencing scheme. However, this is achieved at the expense of increased difficulties to attain converged solutions, with a strong tendency for oscillations and overshoots especially in regions of sharp stress gradients. A possible cause for those difficulties was then speculated to be a lack of limitation in the value of stresses at a given cell face, which tended to be higher than the corresponding values in surrounding nodes, and the obvious remedy is the imposition of appropriate boundedness criteria. Similar problems have occurred in the past in the solution of hyperbolic equations for compressible flow in Newtonian fluid mechanics and a number of higher-order schemes were combined and bounded with flux limiters in what became known as high-resolution schemes (Harten [23], Leonard [24]). More recently, the normalised variable formulation introduced by Leonard [24] has been extended to handle non-uniform mesh spacing in the context of the normalised variable and space formulation (NVSF) of Darwish and Moukalled [25], which is followed in this work.

In the NVSF the convected stress component τ_{ij} (or any other convected variable ϕ) and the general curvilinear co-ordinate ξ are normalised as

$$\widehat{\tau}_{ij} = \frac{\tau_{ij} - \tau_{ij,\mathrm{U}}}{\tau_{ij,\mathrm{D}} - \tau_{ij,\mathrm{U}}}, \tag{7}$$

$$\widehat{\xi} = \frac{\xi - \xi_{\mathrm{U}}}{\xi_{\mathrm{D}} - \xi_{\mathrm{U}}}, \tag{8}$$

where the subscripts U and D refer to the upstream and downstream cells to cell P which is the cell immediately upstream of cell face 'f' under consideration. To satisfy the convection boundedness criterion (CBC) of Gaskell and Lau [26] the functional relationship of an interpolation scheme applied to a cell face 'f', $\widehat{\tau}_{ij,\mathrm{f}} = \mathrm{fn}(\widehat{\tau}_{ij,\mathrm{P}})$, must be continuous and bounded from below by $\widehat{\tau}_{ij,\mathrm{f}} = \widehat{\tau}_{ij,\mathrm{P}}$ and from above by 1 in the range $0 < \widehat{\tau}_{ij,\mathrm{P}} < 1$. For the ranges $\widehat{\tau}_{ij,\mathrm{P}} \leq 0$ and $\widehat{\tau}_{ij,\mathrm{P}} \geq 1$ the functional must equal $\widehat{\tau}_{ij,\mathrm{P}}$. This criterion is represented by the shadowed region in the normalised variable diagram of Fig. 1(a) and the straight line of slope 1 outside the triangle.

In this work, two high-resolution schemes were implemented and assessed: the MINMOD of Harten [23], combining the second-order upwind scheme (LUDS) and the central differencing scheme (CDS); and the SMART of Gaskell and Lau [26], which is a bounded version of the quadratic upwind scheme (QUICK) of Leonard [27]. In isolation, these high-order differencing schemes fail to satisfy the convection boundedness criterion (see Fig. 1(a), but if appropriately combined as in these two high-resolution schemes, they become bounded. Using the NVSF formulation MINMOD and SMART are expressed analytically by Eqs. (9) and (10) and are represented in Fig. 1(b) as dotted and full lines, respectively.

$$\widehat{\tau}_{ij,\mathrm{f}} = a + b\widehat{\tau}_{ij,\mathrm{P}} = \begin{cases} \dfrac{\widehat{\xi}_{\mathrm{f}}}{\widehat{\xi}_{\mathrm{P}}}\widehat{\tau}_{ij,\mathrm{P}}, & 0 < \widehat{\tau}_{ij,\mathrm{P}} < \widehat{\xi}_{\mathrm{P}} \quad \text{(LUDS)}, \\ \dfrac{1-\widehat{\xi}_{\mathrm{f}}}{1-\widehat{\xi}_{\mathrm{P}}}\widehat{\tau}_{ij,\mathrm{P}} + \dfrac{\widehat{\xi}_{\mathrm{f}} - \widehat{\xi}_{\mathrm{P}}}{1-\widehat{\xi}_{\mathrm{P}}}, & \widehat{\xi}_{\mathrm{P}} \leq \widehat{\tau}_{ij,\mathrm{P}} < 1 \quad \text{(CDS)}, \\ \widehat{\tau}_{ij,\mathrm{P}}, & \text{elsewhere} \quad \text{(UDS)}, \end{cases} \tag{9}$$

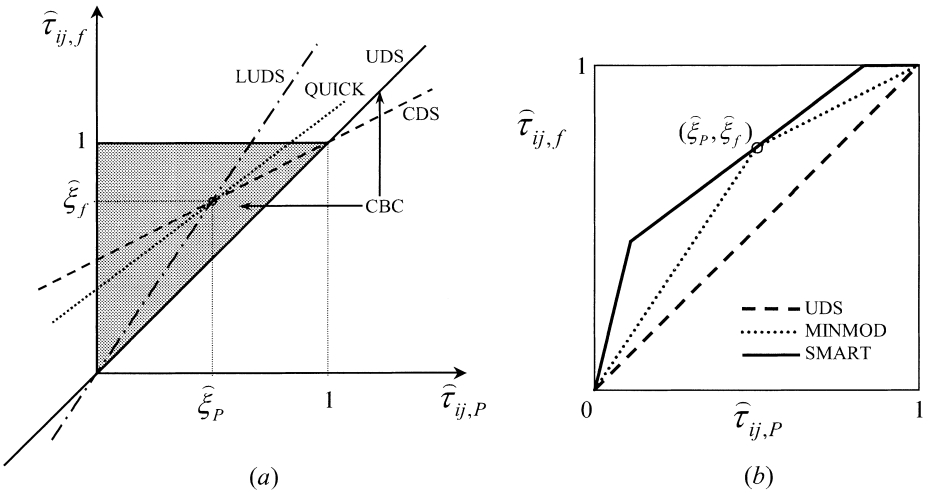

Fig. 1. Representation of the differencing schemes in the normalised variable and space formulation: (a) single interpolation schemes; (b) high-resolution schemes.

$$\widehat{\tau}_{ij,\mathrm{f}} = a + b\widehat{\tau}_{ij,\mathrm{P}} = \begin{cases} \dfrac{\widehat{\xi}_\mathrm{f}(1-3\widehat{\xi}_\mathrm{P}+2\widehat{\xi}_\mathrm{f})}{\widehat{\xi}_\mathrm{P}(1-\widehat{\xi}_\mathrm{P})}\widehat{\tau}_{ij,\mathrm{P}}, & 0 < \widehat{\tau}_{ij,\mathrm{P}} < \dfrac{\widehat{\xi}_\mathrm{P}}{3}, \\ \dfrac{\widehat{\xi}_\mathrm{f}(1-\widehat{\xi}_\mathrm{f})}{\widehat{\xi}_\mathrm{P}(1-\widehat{\xi}_\mathrm{P})}\widehat{\tau}_{ij,\mathrm{P}} + \dfrac{\widehat{\xi}_\mathrm{f}(\widehat{\xi}_\mathrm{f}-\widehat{\xi}_\mathrm{P})}{1-\widehat{\xi}_\mathrm{P}}, & \dfrac{\widehat{\xi}_\mathrm{P}}{3} \le \widehat{\tau}_{ij,\mathrm{P}} < \dfrac{\widehat{\xi}_\mathrm{P}}{\widehat{\xi}_\mathrm{f}}(1+\widehat{\xi}_\mathrm{f}-\widehat{\xi}_\mathrm{P}) \quad \text{(QUICK)}, \\ 1, & \dfrac{\widehat{\xi}_\mathrm{P}}{\widehat{\xi}_\mathrm{f}}(1+\widehat{\xi}_\mathrm{f}-\widehat{\xi}_\mathrm{P}) \le \widehat{\tau}_{ij,\mathrm{P}} < 1, \\ \widehat{\tau}_{ij,\mathrm{P}}, & \text{elsewhere} \quad \text{(UDS)}. \end{cases} \tag{10}$$

For each scheme, a bit of algebra shows that the convective fluxes in the stress equation can be rewritten as

$$\frac{\lambda}{\rho}F_\mathrm{f}\hat{\tau}_{ij,\mathrm{f}} = \frac{\lambda}{\rho}F_\mathrm{f}\tau_{ij,\mathrm{P}} + \frac{\lambda}{\rho}F_\mathrm{f}[a(\tau_{ij,\mathrm{D}} - \tau_{ij,\mathrm{U}}) + (b-1)(\tau_{ij,\mathrm{P}} - \tau_{ij,\mathrm{U}})]_\mathrm{f}, \tag{11}$$

where the a and b are obtained from Eq. (9) for MINMOD and Eq. (10) for SMART. The factor λ/ρ arises because the F_f are mass flow rates and, as indicated by the convective term in the constitutive equation, these must be transformed into volumetric fluxes and multiplied by the relaxation time. Stress fluxes from Eq. (11) are evaluated for each of the six faces of a cell, are summed (with incoming fluxes taken as negative), and are then incorporated into the source term of the stress equation $S_{\tau_{ij}}$ following the deferred correction approach outlined above. It is known that deferred correction tends to slow down the convergence rate to a steady-state solution and some purpose-built techniques have been developed to

overcome this problem. However, the deferred correction leads to a simpler and more general implementation of convective fluxes together with important memory savings, since the coefficients a_F and a_P are the same for all six stress equations and are readily calculated from the a_F coefficients of the momentum equation, after multiplication by λ/ρ.

3.3. Solution procedure

The discretised sets of equations for each variable are solved sequentially in a decoupled manner and the revised version of the SIMPLEC algorithm [28], as explained in Oliveira et al. [1], is used to ensure conservation of mass and momentum by the pressure and velocity fields. As shown there, the original algorithm is only marginally affected by extension to viscoelastic flow calculations and is independent of the constitutive equation chosen. The algorithm is also not affected by the adoption of the HR scheme which is introduced through the deferred correction approach, and we refer to [1,18] for further details on the numerical method.

To check for convergence to a steady-state either, the L_1-norm of the residuals of the equations were required to fall below a tolerance of 10^{-4} or the relative change of the solution satisfied

$$\frac{||X^{(n+1)} - X^{(n)}||_2}{||X^{(n+1)}||_2} \leq \delta, \tag{12}$$

where $X^{(n)}$ is the solution vector at time step (n) and δ was set to 10^{-7}. Implicit solution of the linear sets of equations was carried out iteratively with standard pre-conditioned symmetric or bi-conjugate gradient methods [29].

4. Problem description and computational meshes

We consider the plane flow past a circular cylinder placed perpendicularly at the centreline of a channel, as represented schematically in Fig. 2. The ratio of channel half-height h to cylinder radius R is equal to 2. The computational domain is $80R$ long, with $19R$ upstream and $59R$ downstream of the forward and rear stagnation points of the cylinder, respectively.

The upstream domain was sufficiently long to establish fully-developed velocity and stress profiles upstream of the cylinder for both the UCM and Oldroyd-B fluids, although the calculations reported in

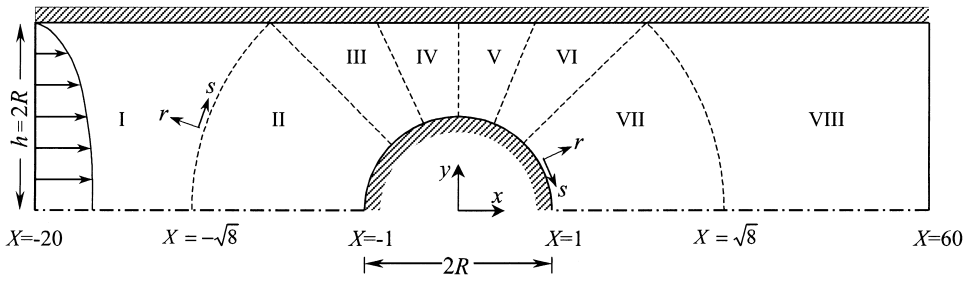

Fig. 2. Schematic representation of the flow geometry and definition of the blocks used to generate the mesh ($X = x/R$). The flow is from left to right.

Section 5 were carried out with imposed fully-developed inlet conditions for velocity and stress. The downstream length is sufficient for the outlet flow to become fully-developed and to avoid any effect of the outlet condition upon the flow in the vicinity of the cylinder. Vanishing axial gradients are applied to all variables, including the pressure gradient, at the outlet plane. No-slip conditions are imposed at both the cylinder surface ($r = R$) and the channel wall ($y = h$) where the stress components are obtained from solution of the constitutive equations.

All the calculations were carried out for the limiting case of $Re = 0$ and this was imposed in the code by equating to zero the convective terms of the momentum equation. Therefore, the remaining relevant non-dimensional quantity is the Deborah number defined in the usual way as

$$De = \frac{\lambda U}{R}, \tag{13}$$

with U representing the bulk velocity in the channel. The inlet bulk velocity was kept constant and the Deborah number was varied by changing the value of the relaxation time. A constant time step of $\delta t = 0.5 \times 10^{-3} R/U$ was used in all calculations for the various Deborah numbers considered; in terms of mesh spacing, it corresponds to a local Courant number of about 0.6 in the finest mesh. The ratio of solvent to total viscosity of the Oldroyd-B fluid was set to be the same as in other works in the literature to enable exact comparison of results, i.e.

$$\frac{\eta_s}{\eta_s + \eta_p} = 0.59. \tag{14}$$

The flow is assumed to have a plane of symmetry along the centreline ($y = 0$) and so only half of the domain needs to be considered. Generation of the block-structured meshes required subdivision of the flow domain into eight blocks as represented in Fig. 2. Within each block the cells were concentrated near the cylinder surface and the centreplane in order to resolve adequately the boundary-layer and downstream wake. In total, six meshes with different degrees of refinement were used, but only the characteristics of the five finer meshes are presented in Table 1.

For the purpose of application of Richardson extrapolation for error estimation, the meshes can be grouped into two sets, (M45,M90) and (M60, M120), where the figures after the M, indicate the number of radial cells between the cylinder and the channel wall. Within each set the refinement was consistent in the sense that the number of cells was doubled in each direction, with grid spacing being approximately halved, following the procedure of Ferziger and Perić [30] for non-uniform meshes. Although mesh doubling is not strictly required to apply Richardson's extrapolation, it facilitates this technique of obtaining error estimates.

An idea of mesh fineness can be grasped from the plot of a medium mesh in the upper part of Fig. 3. The finest mesh has four times more cells than that in Fig. 3. As will become clear later, even this mesh is not sufficiently refined in the tangential direction (s) to resolve the build-up of normal stresses in the wake, at the back of the cylinder. For this reason, a corresponding wake-refined mesh (M60 (WR)) has been created and is shown in the lower part of Fig. 3; it has roughly the same characteristics of M60, but the minimum tangential spacing is $(\Delta s/R)_{\min} = 0.000613$, compared with 0.0157 for M60. Mesh M60WR will only be used to study the details of the stress wake.

Table 1
Main characteristics of the meshes (NS × NR per block)[a]

Block	M45	M60	M75	M90	M120
I	38 × 36	50 × 48	62 × 60	75 × 72	100 × 96
II	38 × 45	50 × 60	62 × 75	75 × 90	100 × 120
III	19 × 45	25 × 60	31 × 75	38 × 90	50 × 120
IV	19 × 45	25 × 60	31 × 75	38 × 90	50 × 120
V	19 × 45	25 × 60	31 × 75	38 × 90	50 × 120
VI	19 × 45	25 × 60	31 × 75	38 × 90	50 × 120
VII	38 × 45	50 × 60	62 × 75	75 × 90	100 × 120
VIII	38 × 45	50 × 60	62 × 75	75 × 90	100 × 120
NCV	9918	17400	26970	39330	69600
$(NS)^{tot}$	152	200	248	302	400
$(\Delta r/R)_{min}$[b]	0.00646	0.00481	0.00383	0.00318	0.00238
$(\Delta s/R)_{min}$[b]	0.0207	0.0157	0.0127	0.0104	0.00785

[a] NCV: total number of control volumes; NS, NR: number of cells in tangential and radial directions; $(NS)_{tot}$: number of tangential cells around half-cylinder.
[b] Smallest cell all around the cylinder surface.

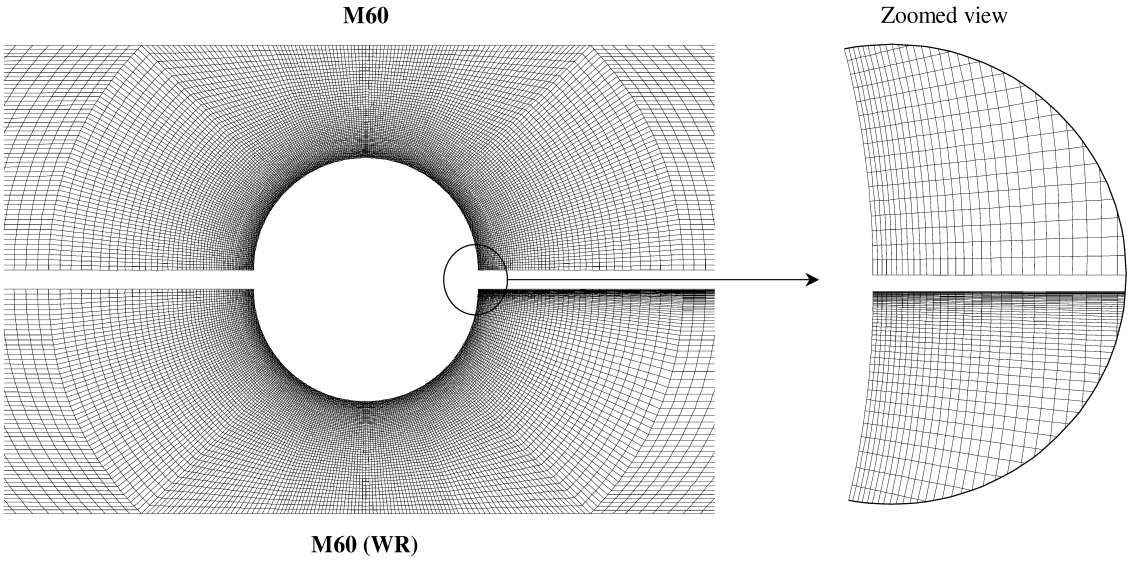

Fig. 3. Meshes M60 and M60WR (wake-refined) in the vicinity of the cylinder.

5. Results and discussion

Results of the computations are presented in two ways: a scalar integral quantity representative of the flow, and detailed profiles of velocities and stress components in the vicinity of the cylinder. The integral quantity is the dimensionless drag coefficient C_d resulting from surface integration of the stress

and pressure fields around the cylinder:

$$C_{\mathrm{d}} \equiv \frac{1}{\eta U}\int_S (\boldsymbol{\tau}_{\mathrm{tot}} - p\boldsymbol{I}) \cdot \boldsymbol{n} \cdot \hat{\boldsymbol{i}}\, \mathrm{d}S, \tag{15}$$

where $\boldsymbol{I}$ is the identity tensor, $\boldsymbol{n}$ the unit normal vector to the cylinder surface and $\hat{\boldsymbol{i}}$ is the unit vector in the x-direction.

Correct predictions of integral quantities is not always synonymous of accurate predictions of the velocity and stress fields, because local variations of these quantities may compensate each other and the errors be convected away. Therefore, velocity and stress profiles in the difficult thin stress boundary-layer and rear wake along the centreplane will also be shown in order to ascertain the quality of the predictions. The results will be compared with very recent data from the literature, most from 1999 [8–11,31]. We start by estimating the order of convergence of the various differencing schemes based on results of the drag force for all cases that were simulated, Section 5.1. Then results are given separately for the UCM (Section 5.2) and Oldroyd-B fluid models (Section 5.3).

5.1. Order of convergence

The predicted C_{d} values are listed in Tables 2 and 3 for the UCM and Oldroyd-B fluids, respectively, and some data from the literature are given for comparison. Under the column "Extrapolation", Tables 2 and 3 give values of the drag coefficient obtained from application of Richardson's extrapolation to the limit technique after determination of the order of convergence of the calculations. The order of convergence was obtained in two different, but related, procedures. In one of them, also used by Liu et al. [8], C_{d} was plotted as a function of the minimum grid spacing Δr and a least square fit of

$$C_{\mathrm{d}} = C_{\mathrm{d_{extr}}} + b(\Delta r)^n \tag{16}$$

gave the extrapolated drag coefficient $C_{\mathrm{d_{extr}}}$ and the order of convergence n. A simpler trial and error method assumes that the extrapolated C_{d} from Richardson's technique represents the exact (reference) solution and plots the variation of the estimated error $|C_{\mathrm{d}} - C_{\mathrm{d,ref}}|$ as a function of $(\Delta r/R)_{\min}$ in log–log coordinates, the slope of which then gives the order of convergence, as shown in Fig. 4. As an estimate of the exact C_{d} taken as a reference value, $C_{\mathrm{d,ref}}$, the extrapolated value from the SMART calculations was used in all cases, as that was the most accurate scheme in this study. Fig. 4 also demonstrates that the asymptotic range of C_{d} is achieved in the four finer meshes, for the relatively high $De = 0.9$ and for both the UCM and Oldroyd-B fluids. The orders of convergence of the various methods were, thus, determined and are listed in Table 4: second-order for MINMOD and SMART, with SMART slightly more accurate than MINMOD, and first-order for UDS.

5.2. Upper convected Maxwell fluids

Fig. 5(a) compares our extrapolated values of C_{d} with those of Fan et al. [9], obtained with FEM and their MIX1 formulation, and with the CVFEM results of Phan-Thien and Dou [31]. The present extrapolated curves based on results with the SMART and MINMOD high-resolution schemes basically collapse, with small differences only discernible in the tabulated form. There is excellent agreement between ours and Fan et al.'s. [9] predictions, who used a very accurate FEM h-p refinement technique (with polynomials of up to sixth order), and both sets are well below the predictions of Phan-Thien and Dou [31]. These

Table 2
Drag coefficient for UCM fluids

De	M45	M60	M75	M90	M120	Extrapolation	Fan et al. [9] MIX 1	Fan et al. [9] DEVSS	Interpolation scheme
0	132.23[a]	132.342			132.369	132.378	132.36	132.36	SMART
0.01		132.080			132.225	132.370			UDS
		132.129			132.250	132.291			MINMOD
		132.132			132.251	132.291			SMART
0.025		131.688			131.878	132.069			UDS
		131.809			131.941	131.985			MINMOD
		131.817			131.945	131.988			SMART
0.05		130.534			130.786	131.038			UDS
		130.768			130.907	130.953			MINMOD
		130.780			130.912	130.956			SMART
0.1		126.799			127.141	127.483			UDS
		127.203			127.347	127.395			MINMOD
		127.224			127.356	127.400	127.41	127.42	SMART
0.2		117.077			117.485	117.893			UDS
		117.615			117.751	117.796			MINMOD
		117.645			117.767	117.808	117.81	117.83	SMART
0.3	107.806	108.043	108.178	108.264	108.385	108.727			UDS
	108.387	108.484	108.534	108.566	108.600	108.639			MINMOD
	108.444	108.515	108.555	108.582	108.614	108.647	108.66	108.68	SMART
0.4		101.134			101.300	101.466			UDS
		101.265			101.344	101.370			MINMOD
		101.287			101.361	101.385	101.41	101.43	SMART
0.5		96.390			96.275	96.160			UDS
		95.984			96.030	96.045			MINMOD
		95.987			96.037	96.054	96.08	96.11	SMART
0.6		93.467			92.970	92.473			UDS
		92.302			92.306	92.307			MINMOD
		92.277			92.298	92.305	92.33	92.37	SMART
0.7		91.973			90.995	90.017			UDS
		89.857			89.799	89.780			MINMOD
		89.796			89.774	89.767	89.79	89.84	SMART
0.8		91.578			90.039	88.500			UDS
		88.359			88.207	88.156			MINMOD
		88.253			88.178	88.153		88.18	SMART
0.9	93.113	92.029	91.221	90.581	89.856	87.683			UDS
	87.850	87.585	87.452	87.373	87.277	87.174			MINMOD
	87.590	87.395	87.325	87.268	87.218	87.160			SMART
1.0		93.063			90.268	87.473			UDS
		87.272			86.750	86.576			MINMOD
		87.05			Note[b]	Note[b]			SMART
1.1		94.630			90.995	87.360			UDS
		87.355			Note[b]	Note[b]			MINMOD
1.2		96.828			Note[b]	Note[b]			UDS
1.3		98.942							UDS
1.4		102.060							UDS
1.5		104.575							UDS

[a] With M30.
[b] Not converged.

Table 3
Drag coefficient for Oldroyd-B fluids[a]

De	M45	M60	M75	M90	M120	Extrapolation	Fan et al. [9] MIX 1	Sun et al. [10] DAVSS	Liu et al. [8] DEVSS	Dou and Phan-Thien [11] DAVSS-ω
0							132.36	132.34	132.34	131.81
0.01		132.282			132.336	132.354				
0.025		132.156			132.209	132.227				
0.05		131.735			131.788	131.806				
0.1		130.307			130.343	130.355	130.36			129.72
0.2		126.575			126.618	126.632	126.62			126.41
0.3	123.107	123.151	123.175	123.185	123.195	123.210	123.19			123.52
0.4		120.564			120.596	120.607	120.59			121.56
0.5		118.814			118.832	118.838	118.83	119.11	119.48	120.58
0.6		117.782			117.786	117.787	117.77	118.17	118.72	120.49
0.7		117.344			117.328	117.323	117.32	117.84	118.54	121.13
0.8		117.410			117.370	117.357	117.36			122.57
0.9	117.948	117.907	117.888	117.876	117.865	117.851	117.79			124.48
1.0		118.685			118.56	118.518	118.49	119.32	119.47	126.89

[a] All calculations with SMART.

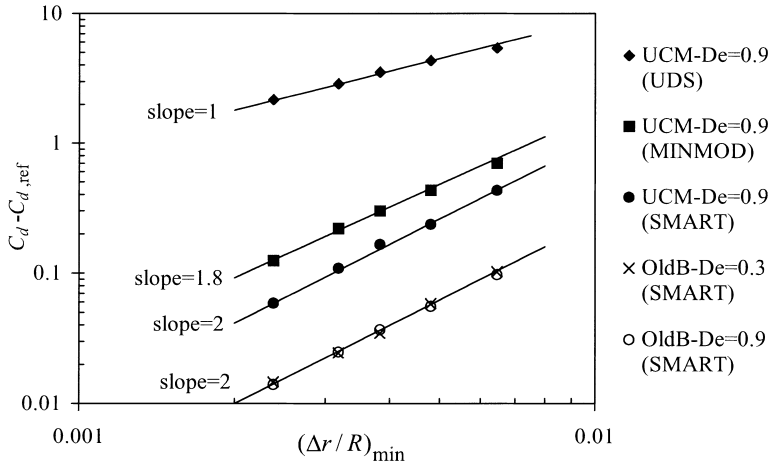

Fig. 4. Estimated error vs. minimum cell size.

Table 4
Order of convergence of the numerical simulations

De	UCM			OLD-B
	UDS	MINMOD	SMART	SMART
0.3	1.1	1.9	2.0	2.0
0.9	1.0	1.8	2.0	2.0

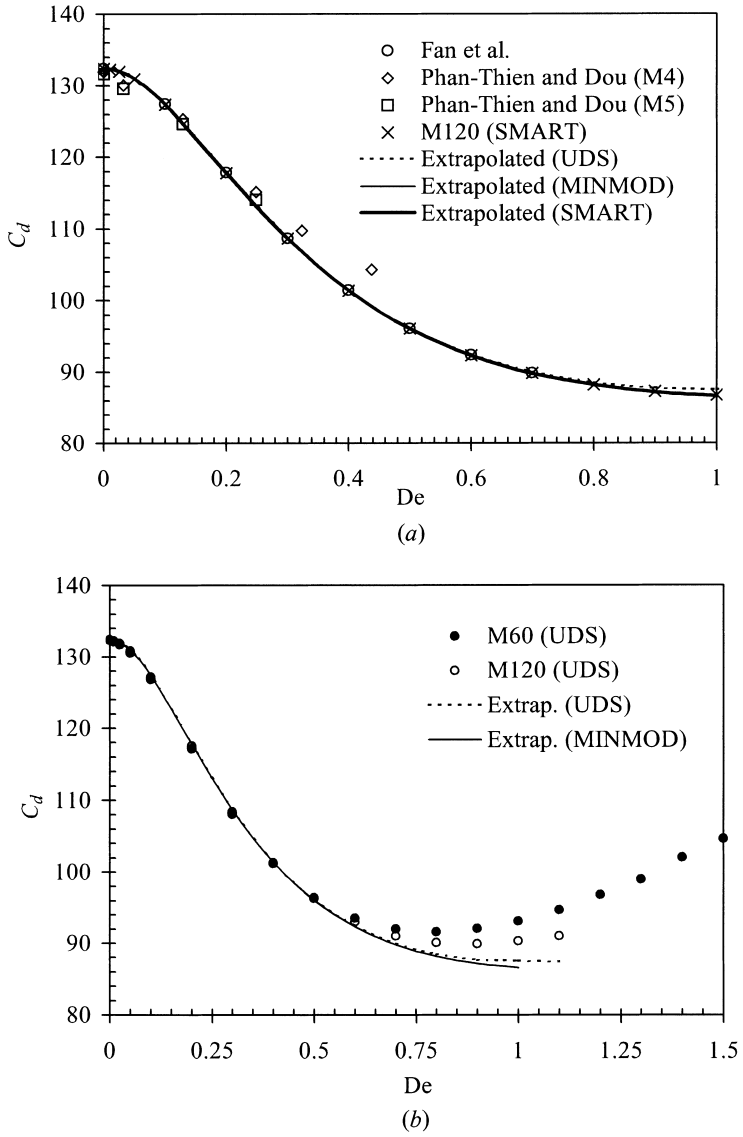

Fig. 5. Drag coefficient as a function of the Deborah number for UCM fluids: (a) comparison with data from the literature; (b) predictions with the upwind scheme (UDS).

authors do not give details of the "equal-order" weighting functions they used to interpolate the convective terms in their CVFEM, but presumably they are only first-order accurate, like the exponential form of the original CVFEM formulation (see e.g. Patankar [32]). As shown in Fig. 5(b), their results seem worst then ours with the upwind scheme (UDS, which is also first-order, see Table 4) and they fail to obtain converged solutions for $De > 0.43$, whereas we could go up to $De = 1.5$ in the medium mesh M60.

An assessment of the improved accuracy induced by the high-resolution schemes over the whole range of *De* is best illustrated in a plot of the relative difference in the predicted drag coefficient values versus

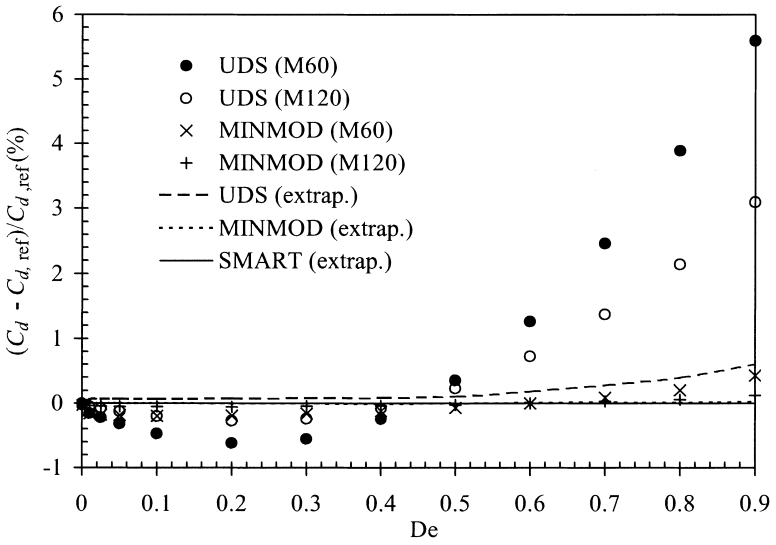

Fig. 6. Percent difference in drag coefficient relative to the most accurate extrapolated value (with SMART).

De (Fig. 6). The reference C_d value used to evaluate the relative differences is taken as the best prediction, obtained from Richardson's extrapolated values with the SMART scheme. In the range $De \leq 0.5$ there is good agreement between all predictions, although the UDS predictions do show already somewhat lower accuracy, with differences in excess of 0.6%. For Deborah numbers above 0.5 the predictions with UDS deteriorate considerably and more so as *De* increases. For example, at $De = 0.7$, the relative difference rises to 2.5 and 1.4% in meshes M60 and M120, respectively. However, even for this *De* the difference is not so high (just 0.3%) if we take the extrapolated UDS values, instead of the fine mesh UDS predictions. With the high-resolution schemes the differences are always low, e.g. 0.07% in M120 and 0.3% in M60 at $De = 0.9$ with SMART.

What is evident from both Figs. 5 and 6 is that, as *De* increases, the inaccuracies in the predicted C_d with the lower order scheme tend to progressively increase, the C_d value itself tends to be higher than the "exact" solution and, furthermore, it starts increasing whereas the best predictions show an asymptotic minimum level of C_d for high *De*.

Profiles of the axial velocity along the centreline ($y = 0$) for Newtonian and UCM fluids at increasing *De* are compared in Fig. 7. As expected the Newtonian flow exhibits a symmetric velocity profile, but this symmetry is broken for $De \neq 0$ as elasticity tends to elongate the recovery zone, except in the near vicinity of the rear stagnation point (see the inset in Fig. 7). The profiles in Fig. 7 are mesh-independent as well as independent of the high-resolution scheme since both MINMOD and SMART result in practically coincident predictions in meshes M60 and M120. Fig. 7 suggests a downstream shift of the streamlines, as compared with the Newtonian case, except close to the back of the cylinder where an upstream shift, that increases in magnitude, but decreases in physical size with Deborah number, is observed. Streamlines for the UCM are not significantly different from those for the Oldroyd-B fluid, except that the upstream shift of the latter is more pronounced, and thus, we delay their study to the next Section 5.3 dealing with the Oldroyd-B.

Normal stress profiles around the cylinder and along the centreline are plotted in Fig. 8, and two maxima are observed. The first maximum is within the thin boundary layer over the cylinder surface and the second

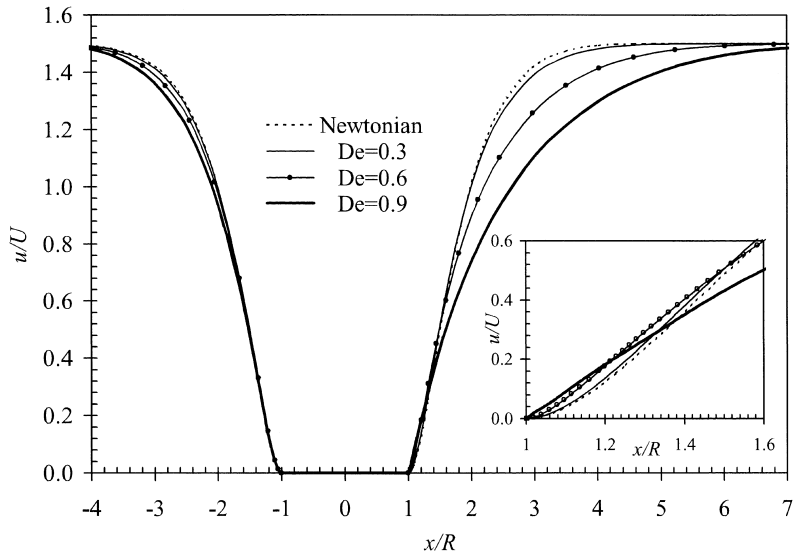

Fig. 7. Profiles of longitudinal velocity along centreline for UCM fluids: effect of *De*.

maximum is in the wake, some distance downstream from the rear stagnation point. It is apparent from Fig. 8 that the increase of the boundary-layer maximum stress is progressively smaller as the Deborah number increases, whereas the wake-maximum is progressively larger. Similar observations of this different behaviour of the longitudinal normal stress maxima have been reported by Fan et al. [9] who related the growth of the wake-maximum with breakdown of the calculations at high Deborah numbers. In this respect

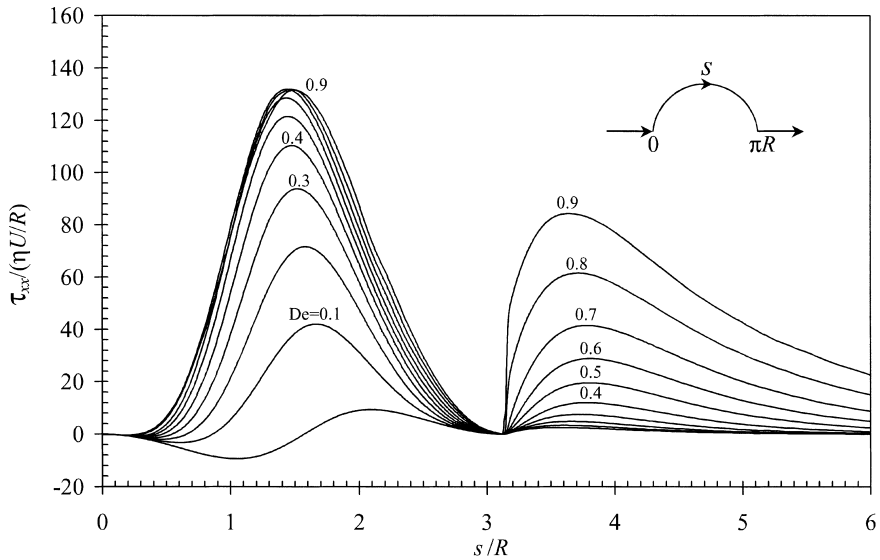

Fig. 8. Profiles of longitudinal normal stress (τ_{xx}) along cylinder wall and wake centreline for UCM fluid at increasing *De* (mesh M120; SMART scheme).

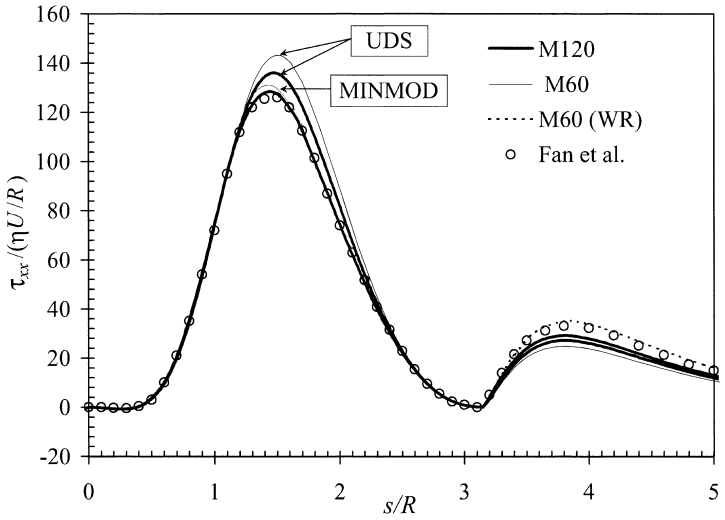

Fig. 9. Influence of interpolation scheme and mesh refinement on the predictied τ_{xx} along cylinder wall and wake centreline, and comparison with Fan el al. [9] predictions ($De = 0.6$).

the present numerical method shows somewhat more robustness, in spite of being a decoupled procedure: we were able to obtain converged solutions with the high-resolution schemes MINMOD and SMART up to $De = 1$ and 0.9, respectively, whereas the MIX1 calculations of Fan et al. diverged for $De > 0.75$.

At the moderate value of $De = 0.6$, our longitudinal normal stress predictions are very close to those of Fan et al., as shown in Fig. 9, except in the stress wake, where the predictions with the fine mesh M120 fall somewhat lower. However, by refining the mesh in that area (M60 WR), especially in the direction tangential to the cylinder surface (that is, the θ-direction for a cylindrical coordinate system centred in the cylinder axis), we are then able to match closely Fan et al.'s predictions in the wake. Fig. 9 also demonstrates the improved convergence and accuracy brought about by the high-resolution schemes. The MINMOD predictions are far less affected by mesh fineness and are in better agreement with the high-order h-p FEM results of Fan et al. Agreement in the stress boundary layer around the cylinder is reflected in the coincidence of C_d values exhibited in the previous section. It is, however, in the wake region that convergence problems are first apparent at higher *De*. Fan et al. [9] observed that their results for τ_{xx} in the wake were no longer h-p independent at $De \approx 0.7$ (after which iterative convergence broke down), and that is precisely the *De*-range where our τ_{xx} results start deviating from theirs, as inspection of the variation of $\max(\tau_{xx})$ will elucidate. The variation of the two stress maxima with *De* is shown in Fig. 10 and the figure shows that mesh-independence of the results deteriorates as the *De* number is increased especially in the wake region. The boundary layer maximum tends to an asymptotic value which is well captured by the M120 calculations and that is reflected in the good agreement between C_d predictions. On the other hand, the wake-maximum increases non-linearly with the Deborah number. These τ_{xx} stress maxima occur at the centreline ($\theta = 0$, or $y = 0$) and therefore higher rates-of-increase and maximum values are predicted as the meshes are more and more refined in that area (going from M60, to M120, to M60 WR). In the wake-refined mesh, M60WR, our predictions of the second τ_{xx} maximum compare very well with those of Fan et al. up to $De = 0.75$, above which Fig. 10 shows a tendency for the second maximum to overcome the first maximum, and the predictions diverge. The asymptotic behaviour

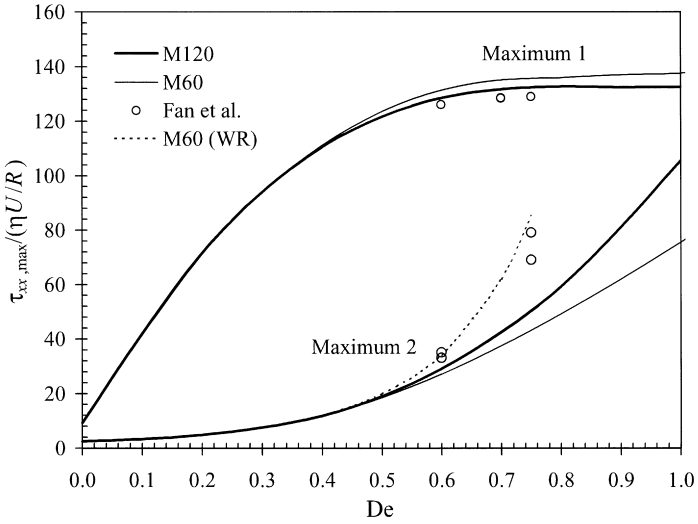

Fig. 10. Variation of the two maximum values of τ_{xx} with *De* for UCM fluids. Maximum 1: in boundary layer; maximum 2: in stress wake behind cylinder.

of the τ_{xx} stresses with the azimuthal angular position is shown in Fig. 11, for increased *De* and in meshes M120 and M60WR. These profiles are at a fixed distance from the cylinder (*r*, constant) corresponding to the location of maximum τ_{xx} in the wake for each *De*. Fig. 11 shows that M120 does a good job in predicting the correct τ_{xx} up to the last cell closer to the centreline, but since τ_{xx} is still growing, more mesh refinement in θ will produce higher τ_{xx} (especially for $De \geq 0.7$). The figure indicates that for $De \leq 0.6$, τ_{xx} tends asymptotically to a constant value with diminishing θ, but for higher *De* ($De \geq 0.75$) τ_{xx} will tend to infinity as θ decreases to zero. Hence the numerical results for high *De* suggest that a stress singularity develops along the wake, at least in the position where τ_{xx} reaches a local maximum value (the second maximum referred to in relation to Fig. 8), and the iterative-like scheme breaks down as one tries to resolve it (with locally wake-refined meshes). It is not clear whether such "singularity" is of physical

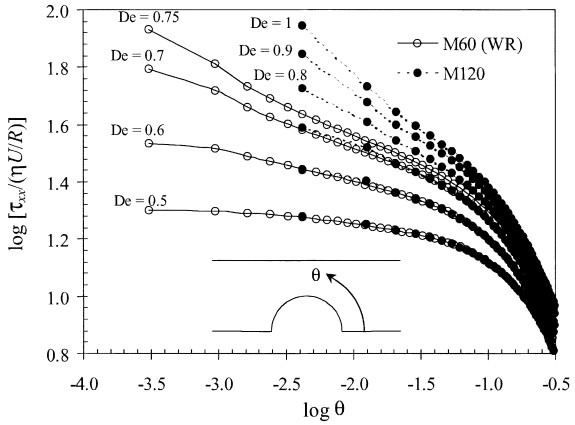

Fig. 11. Asymptotic behaviour of the normal stress with the azimuthal position for increased elasticity.

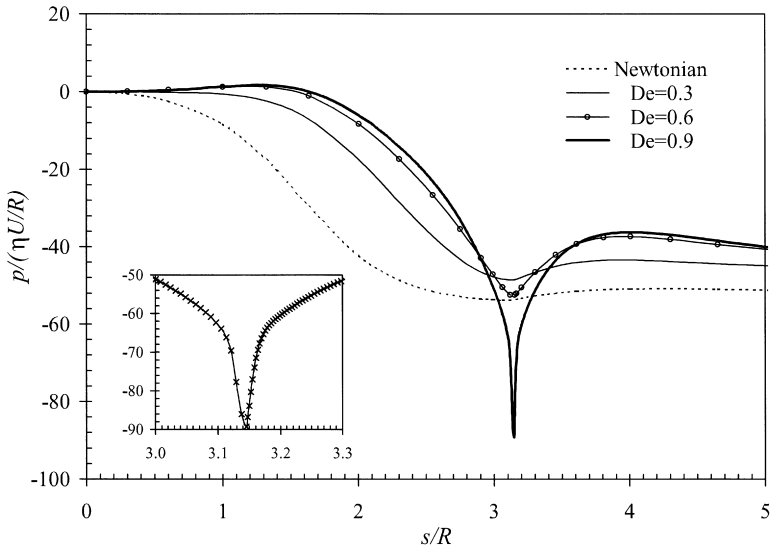

Fig. 12. Influence of Deborah number on the pressure distribution around the cylinder surface and along the wake centreline (UCM; SMART scheme; $p = 0$ at forward stagnation point).

origin for a fluid obeying the UCM model, or if it is an outcome of the numerical procedure. Sun et al. [10] also report the possibility of singular behaviour of the stress field in the wake for the Oldroyd-B fluid. On the other hand Luo [33], based on a semi-analytical solution for the τ_{xx} evolution along the centreline, argues that τ_{xx} should be bounded provided $\partial u/\partial x$ does not change sign. However, in his derivation Luo did not consider the coupling between the simplified τ_{xx} equation and the axial momentum equation, which would give rise to a non-linear differential equation for τ_{xx} not amenable to analytic solution.

Another possible cause for the numerical problems leading to convergence breakdown could be related to the pressure variation around the cylinder wall and centreline, which is shown for various *De* in Fig. 12. As *De* increases the pressure on the cylinder rear surface increases progressively, but smoothly, due to the shifted flow pattern and results in the reduced drag. Within the rear stagnation point region a different situation arises: at low Deborah numbers the pressure level tends to rise steadily with *De*. At a critical Deborah number between 0.3 and 0.6 the behaviour of the rear stagnation point pressure reverses: a point of highly-negative peak pressure develops and becomes more pronounced as *De* increases. At high *De* ($De \approx 0.9$) that point has developed into a wake singularity.

While Fig. 7 shows that the velocity field for the elastic cases is different from the Newtonian case, it is interesting to compare our results with the recent asymptotic analysis of Renardy [34] which predicts stresses in the wake of order De^3 and a localised area near the cylinder of larger stresses, of order De^5. In Fig. 13 we plot in log–log scale the variation of the τ_{xx} wake-maximum with *De*, based on simulations with progressively wake-refined meshes, M60, M120, M60WR. The results with the finest mesh in the wake M60WR show two asymptotic zones: for lower *De* the maximum stresses grow as De^3, and for higher *De* they grow as De^5. When the meshes are not sufficiently refined in the wake, the rate-of-growth of τ_{xx} in the high *De*-zone is not so pronounced, but tends to increase with mesh refinement ($\propto De^2$ in M60 and $\propto De^{2.6}$ in M120).

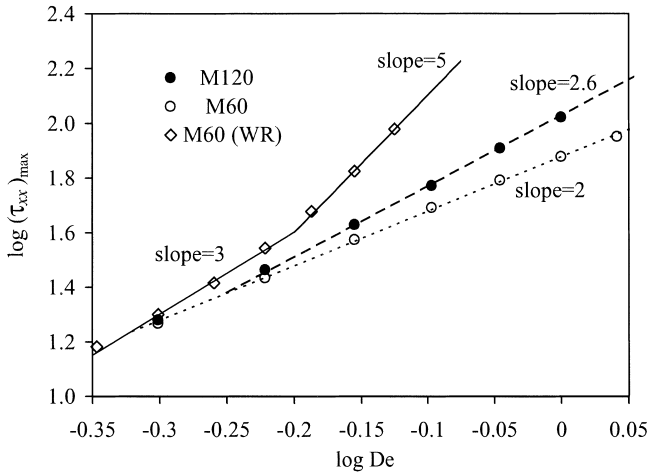

Fig. 13. Asymptotic variation of the maximum normal stress component τ_{xx} in the wake as a function of *De*, in three meshes.

5.3. Oldroyd-B fluids

For the Oldroyd-B fluid the calculations have been carried out with the SMART scheme only since it is the most accurate, and the drag coefficient predictions are compared with the FEM results of: Fan et al. [9] with the MIX1 formulation; Sun et al. [10] with the DAVSS-G/DG formulation; Liu et al. [8] with the DEVSS-G/SUPG formulation; and Dou and Phan-Thien [11] with the CVFEM method and the DAVSS-ω formulation. These data are given in Table 3.

The C_d results of Table 3 are plotted in Fig. 14 and again there is excellent agreement between the finer mesh predictions (both M60 and M120), our Richardson's extrapolated results (not far from the

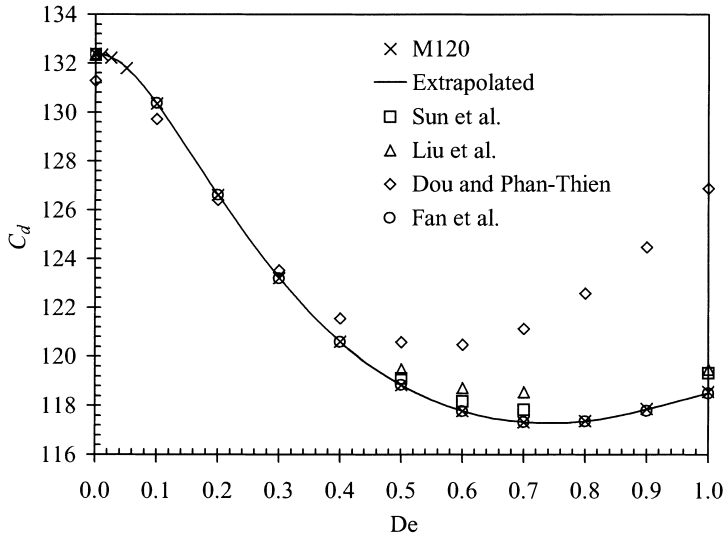

Fig. 14. Drag coefficient as a function of Deborah number for Oldroyd-B fluids.

M120 results), and the FEM predictions of Fan et al. [9] (differences below 0.1%, often below 0.01%). The loss of accuracy of the CVFEM method of Dou and Phan-Thien [11] is apparent for $De \geq 0.3$, and the FEM predictions of the MIT group, Liu et al. [8] and Sun et al. [10], are just somewhat higher for $De \geq 0.5$. Sun et al. [10], who used a FEM with quadratic continuous polynomials for the velocity and linear for the pressure fields, have shown their method to be second-order accurate in a lower blockage cylinder flow ($h/R = 8$) at low Deborah numbers ($De \leq 1.0$). For the present 50% blockage ratio their smallest mesh size is only $\Delta s/R_{\min} = 0.056$ and improvements in their predictions would require further refinement especially at high Deborah numbers. Other possible reason for the discrepancy in Fig. 14 is that the piecewise-linear discontinuous interpolation they used for the stresses in their discontinuous Galerkin approximation tends to be less accurate at higher *De*.

It is interesting to note that if we define a Weissenberg number as $We = \lambda\dot{\gamma}$, with $\dot{\gamma} = U_0/(h-R)$ where U_0 is the average velocity in the constricted gap between cylinder and wall ($h-R$), then for two different aspect ratios ($H \equiv h/R$) we obtain the ratio $We_1/We_2 = H_1(H_2-1)^2/(H_1-1)^2H_2$; for the aspect ratios of 2 and 8 used by Sun et al. this gives $We_1/We_2 = 12$ and so a maximum achievable *De* of 1 at $h/R = 2$ corresponds to a maximum of $De = 12$ at $h/R = 8$. These values are in approximate agreement with the limiting Deborah numbers attained by Sun et al. for the two aspect ratio cases; it also means that the value of $De = 1$ up to which they found their method to be second-order in the $H = 8$ case, is expected to be substantially smaller for the $H = 2$ case.

A difference between the UCM and Oldroyd-B fluid behaviour is that, whereas with the former the C_d was seen to decrease continuously with the Deborah number, with the Oldroyd-B fluid there is an increase at high Deborah numbers, with a minimum drag coefficient occurring at $De \approx 0.75$. At $De = 1$ all methods still give converged solutions and the literature shows that the calculations are more stable with Oldroyd-B fluids than with UCM fluids.

A detailed comparison of the longitudinal normal stress variation along the centreline and cylinder surface is seen in Fig. 15, at the moderate to high Deborah number of 0.7. The fine mesh (M120)

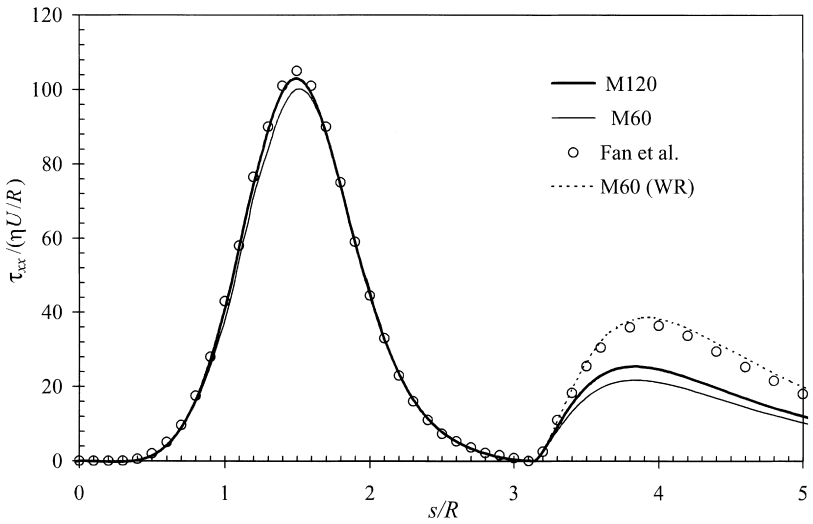

Fig. 15. Influence of mesh refinement on τ_{xx} along cylinder wall and wake centreline, and comparison with literature for Oldroyd-B fluids (SMART scheme; $De = 0.7$).

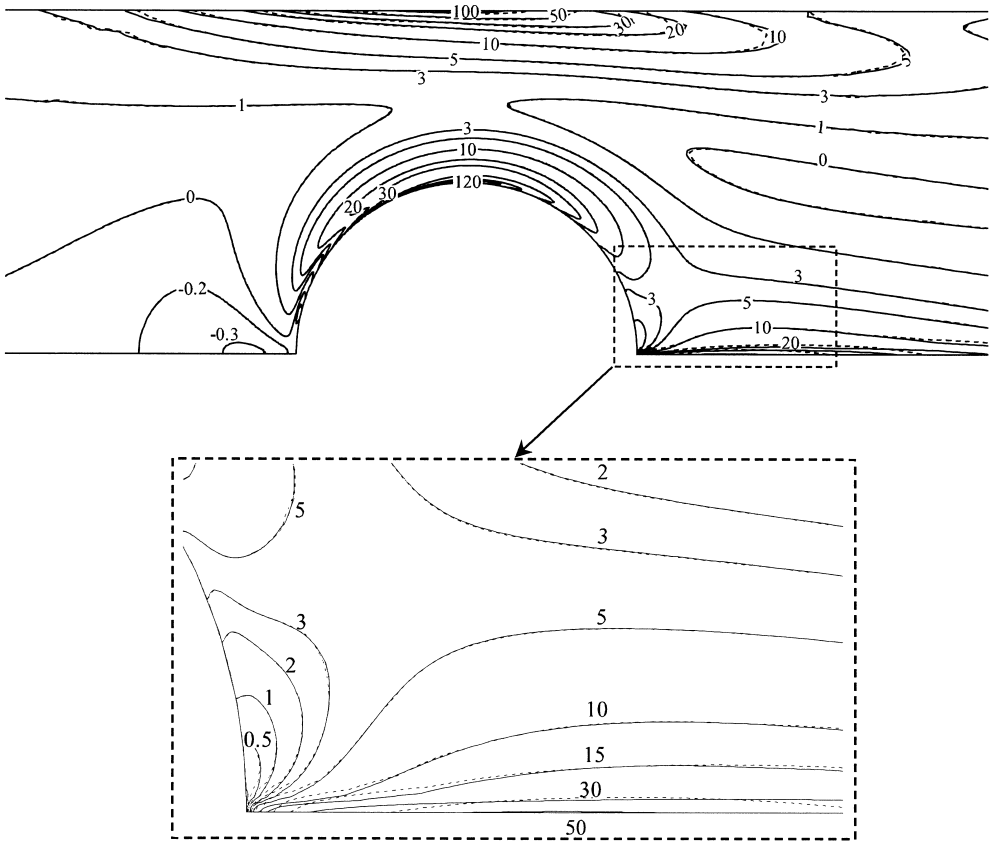

Fig. 16. Comparison of contours of the normal stresses (τ_{xx}) near the cylinder, predicted with mesh M60 (dashed line) and M120 (solid line), at $De = 0.9$.

predictions closely match Fan et al.'s and the difference between M60 and M120 predictions are only apparent near the wake-maximum, where the wake-refined mesh is required to resolve the stress growth and thus, to provide good agreement with Fan et al.'s results. For higher Deborah numbers our C_d still follows Fan et al.'s closely, but the discrepancies in the wake region near the point of maximum τ_{xx} are accentuated and we obtain a variation of $\max(\tau_{xx})$ with *De* similar to that for the UCM (cf. Fig. 10). These discrepancies are confined to the near wake region and do not seem to affect the stress field upstream, around the cylinder; in order to clarify this point, we show in Fig. 16 contours of the normal stress component for the high Deborah number of 0.9, as obtained in the medium M60 and fine M120 meshes. Besides the less-problematic region near the upper wall, where some differences are observed between the predictions in the two meshes, it is only in the wake that those predictions do not coincide. In the contour plots, the rather large discrepancies seen in the profiles in Fig. 15 (and Figs. 9 and 10 for the UCM) are almost unnoticed (they are confined to the wake centreline, along $y = 0$).

The velocity and stress fields for the Oldroyd-B model are basically similar to those for the UCM, with the expected tendency for lower stress levels, but there are a few qualitative differences which we point out briefly.

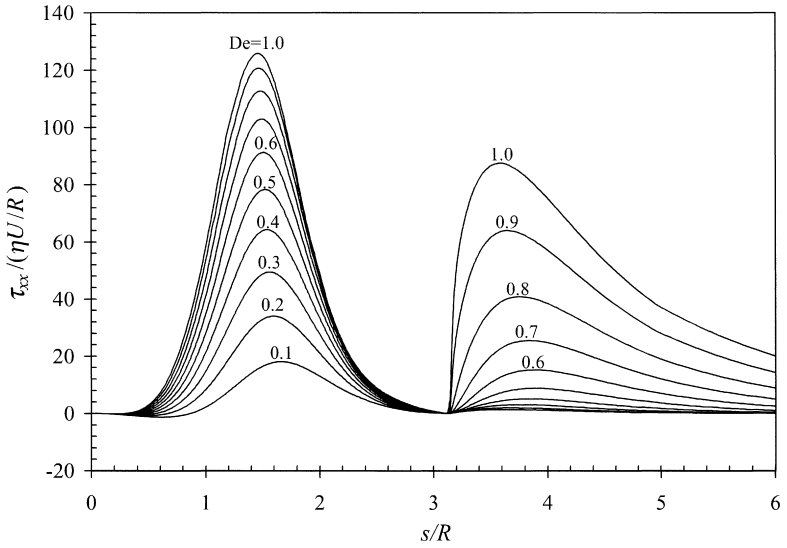

Fig. 17. Profiles of the longitudinal normal stress (τ_{xx}) along cylinder wall and wake centreline for Oldroyd-B fluid (mesh M120; SMART scheme).

Profiles of the longitudinal normal stress along the centreplane and cylinder surface are shown in Fig. 17 for a range of *De*, and this is to be compared with Fig. 8 for the UCM. With the UCM fluid, the maximum τ_{xx} in the cylinder boundary layer is seen to reach its highest values for $De \approx 0.6$–0.7 and remain approximately constant for higher *De*'s, but with the Oldroyd-B fluid the maximum τ_{xx} values

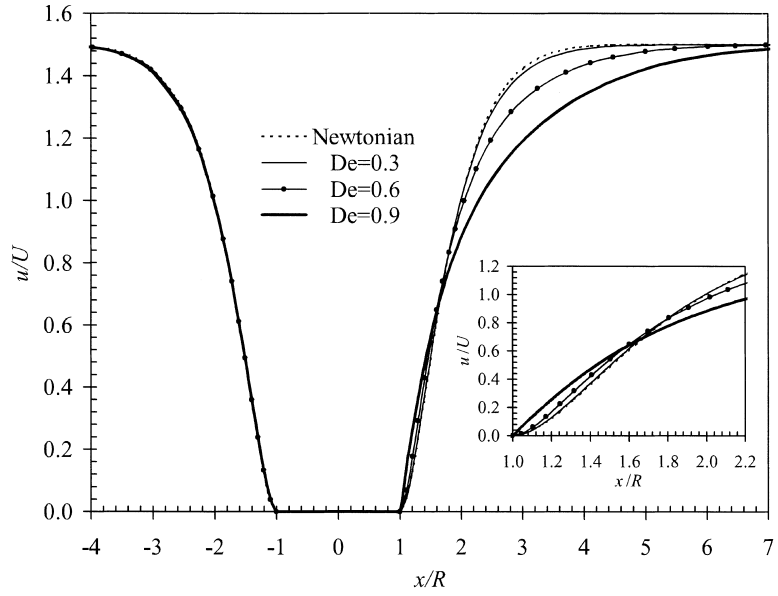

Fig. 18. Profiles of normalised longitudinal velocity along centreline for Oldroyd-B fluids.

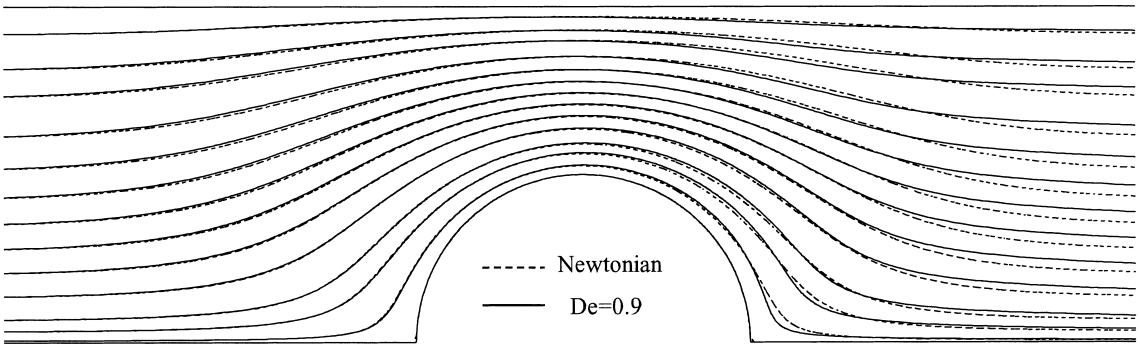

Fig. 19. Zoomed view of the streamlines for a Newtonian fluid (dashed line) and an Oldroyd-B fluid at $De = 0.9$ (full line).

are seen to grow steadily with De. This probably explains the increase of C_d at high Deborah numbers seen in Fig. 14.

Other detailed difference with the UCM is seen in Fig. 18, where the velocity distribution of the Oldroyd-B fluid for the cases $De = 0$, 0.3, 0.6 and 0.9 is plotted along the centreline of the channel. When compared with Fig. 7 for the UCM, we see that the downstream shift of the streamlines is still present far from the back of the cylinder, resulting in the observed decrease of C_d at low and moderate Deborah numbers, but the upstream shift at higher Deborah numbers occurs over a much wider zone close to the rear stagnation point. To clarify these points, streamlines for the Newtonian and one of the Oldroyd-B cases ($De = 0.9$) are shown in Fig. 19, illustrating the downstream shift at the rear stagnation part of the cylinder and in the wake region away from the cylinder, in agreement with other studies, and also the upstream shift in a region closer to the rear stagnation point, as anticipated by the velocity profiles. Similar behaviour has been reported for the corresponding falling-sphere-in-a-tube problem (Bush [35]) and in our previous study for the flow past a cylinder [1].

6. Conclusions

Accurate predictions for the flow around a confined cylinder (blockage ratio 0.5) are obtained with a general collocated FVM incorporating two high-resolution schemes to represent the convective terms in the constitutive equation: MINMOD and SMART. A consistent mesh refinement study and the application of Richardson's extrapolation to the solution functional C_d allowed us to determine the apparent (or observed) order of convergence of the schemes: 2.0 for SMART; 1.8 for MINMOD; and 1.0 for upwind differencing. These estimates are valid in the interval $0 \leq De \leq 0.9$ in which we achieve the asymptotic range for the four finer meshes. The present C_d results can be used as benchmark data with an estimated accuracy in the finer mesh of 0.03% for the UCM and 0.01% for the Oldroyd-B fluids (except for the last available De, for which we obtain 0.07% for UCM at $De = 0.9$, and 0.03% for Oldroyd-B at $De = 1$).

For this problem, which is usually classified under the category of "smooth flow", we have consistent predictions of C_d up to $De \approx 0.7$ between the present FVM and the FEM of Fan et al. [9] who used an highly accurate h-p refinement technique with polynomials of degree up to 6. Other FEM and CVFEM results from the literature start deviating from the present C_d data, and that of [9], at $De \approx 0.3$ (UCM) and

$De \approx 0.4$ (Oldroyd-B), typically exhibiting higher C_d values, an indication of loss of accuracy. It is thus, established that FVM can yield accurate results, provided the discretisation of the constitutive equation and the level of mesh refinement are adequate, in line with opinions vehiculated by Dou and Phan-Thien [11] and Baaijens [36] regarding the need to use higher-order schemes in FVM. In fact, if anything the present decoupled FVM proved to be more robust than the coupled FEM of [9] with solutions for the UCM model up to $De = 1.0$ using MINMOD. However, findings of Fan et al. [9] related to difficulties to attain mesh converged results in the wake of the cylinder at high Deborah numbers are confirmed. In a wake-refined mesh, the maximum τ_{xx} stresses in the wake are seen to increase as De^3 and as De^5 for low and high Deborah numbers, respectively.

Acknowledgements

M.A. Alves is a member of staff at Departamento de Engenharia Química, FEUP, and wishes to thank his colleagues for a temporary leave of absence.

References

[1] P.J. Oliveira, F.T. Pinho, G.A. Pinto, J. Non-Newtonian Fluid Mech. 79 (1998) 1–43.
[2] G.H. Babcock, S. Wilcox, Steam: Its Generation and Use, Babcock & Wilcox, New York, 38th Edition, 1975.
[3] W.M. Rosehnow, Process heat exchangers, in: W.M. Rosehnow, J.P. Hartnett, E.N. Ganic (Eds.), Handbook of Heat Transfer Applications, 2nd Edition, 1985 (Chapter 4).
[4] A. Steiff, K. Klöpper, ASME FED: Part 2, in: Proceedings of the Drag Reduction Symposium, Vol. 237, San Diego, 1996, pp. 235–242.
[5] Y.I. Cho, J.P. Hartnett, Non-Newtonian fluids, in: W.M. Rosehnow, J.P. Hartnett, E.N. Ganic (Eds.), Handbook of Heat Transfer Applications, 2nd Edition, 1985 (Chapter 2).
[6] G. Chauveteau, in: Proceedings of the 56th Annual Fall Technical Conference and Exhibition of the SPE of AIME, San Antonio, TX, 1981, p. 14.
[7] R.A. Brown, G.H. McKinley, J. Non-Newtonian Fluid Mech. 52 (1994) 407–413.
[8] A.W. Liu, D.E. Bornside, R.C. Armstrong, R.A. Brown, J. Non-Newtonian Fluid Mech. 77 (1998) 153–190.
[9] Y. Fan, R.I. Tanner, N. Phan-Thien, J. Non-Newtonian Fluid Mech. 84 (1999) 233–256.
[10] J. Sun, M.D. Smith, R.C. Armstrong, R.A. Brown, J. Non-Newtonian Fluid Mech. 86 (1999) 281–307.
[11] H.-S. Dou, N. Phan-Thien, J. Non-Newtonian Fluid Mech. 87 (1999) 47–73.
[12] X. Huang, N. Phan-Thien, R.I. Tanner, J. Non-Newtonian Fluid Mech. 64 (1996) 71–92.
[13] S.-C. Xue, N. Phan-Thien, R.I. Tanner, J. Non-Newtonian Fluid Mech. 74 (1998) 195–245.
[14] H.H. Hu, D.D. Joseph, J. Non-Newtonian Fluid Mech. 37 (1990) 347–377.
[15] J.Y. Yoo, Y. Na, J. Non-Newtonian Fluid Mech. 39 (1991) 89–106.
[16] G.P. Sasmal, J. Non-Newtonian Fluid Mech. 56 (1995) 15–47.
[17] B. Gervang, P.S. Larsen, J. Non-Newtonian Fluid Mech. 39 (1991) 217–237.
[18] P.J. Oliveira, F.T. Pinho, Num. Heat Transfer Part B 35 (1999) 295–315.
[19] P.J. Oliveira, F.T. Pinho, J. Non-Newtonian Fluid Mech. 88 (1999) 63–88.
[20] M.A. Alves, F.T. Pinho, P.J. Oliveira, J. Non-Newtonian Fluid Mech. 93 (2000) 287–314.
[21] R.I. Issa, P.J. Oliveira, Comput. Fluids 23 (1994) 347–372.
[22] P.K. Khosla, S.G. Rubin, Comput. Fluids 2 (1974) 207–209.
[23] A. Harten, J. Comput. Phys. 49 (3) (1983) 357–393.
[24] B.P. Leonard, Int. J. Num. Meth. Eng. 8 (1988) 1291–1319.
[25] M.S. Darwish, F. Moukalled, Num. Heat Transfer Part B 30 (1996) 217–237.
[26] P.H. Gaskell, A.K.C. Lau, Int. J. Numer. Meth. Fluids 8 (1988) 617–641.

[27] B.P. Leonard, Comp. Meth. Appl. Mech. Eng. 19 (1979) 59–98.
[28] J.P. Van Doormal, G.D. Raithby, Num. Heat Transfer 7 (1984) 147–163.
[29] J.A. Meijerink, H.A. Van Der Vorst, Math. Comput. 31 (1977) 148.
[30] J.H. Ferziger, M. Perić, Int. J. Num. Meth. Fluids 23 (1996) 1263–1274.
[31] N. Phan-Thien, H.-S. Dou, Comput. Methods Appl. Mech. Eng. 180 (1999) 243–266.
[32] S.V. Patankar, Numerical Heat Transfer and Fluid Flow, Mc-Graw Hill, New York, 1980.
[33] X.-L. Luo, J. Non-Newtonian Fluid Mech. 63 (1996) 121–140.
[34] M. Renardy, J. Non-Newtonian Fluid Mech. 90 (2000) 13–23.
[35] M.B. Bush, J. Non-Newtonian Fluid Mech. 49 (1993) 103–122.
[36] F.P.T. Baaijens, J. Non-Newtonian Fluid Mech. 75 (1998) 119–138.